STRUCTURAL BIOLOGY

Structural insights into TRPM8 inhibition and desensitization

Melinda M. Diver[1], Yifan Cheng[2,3]*, David Julius[1]*

The transient receptor potential melastatin 8 (TRPM8) ion channel is the primary detector of environmental cold and an important target for treating pathological cold hypersensitivity. Here, we present cryo–electron microscopy structures of TRPM8 in ligand-free, antagonist-bound, or calcium-bound forms, revealing how robust conformational changes give rise to two nonconducting states, closed and desensitized. We describe a malleable ligand-binding pocket that accommodates drugs of diverse chemical structures, and we delineate the ion permeation pathway, including the contribution of lipids to pore architecture. Furthermore, we show that direct calcium binding mediates stimulus-evoked desensitization, clarifying this important mechanism of sensory adaptation. We observe large rearrangements within the S4-S5 linker that reposition the S1-S4 and pore domains relative to the TRP helix, leading us to propose a distinct model for modulation of TRPM8 and possibly other TRP channels.

Transient receptor potential melastatin 8 (TRPM8) is a cold- and menthol-activated ion channel that plays an essential role in the detection of environmental temperatures (*1*–*5*). It is also targeted by synthetic cooling agents in personal care products and confectionaries (*6*) and by antagonists that may be useful for reducing cold hypersensitivity resulting from nerve damage (*7*, *8*). TRPM8 blockers may also be beneficial in treating chronic cough, asthma, or other airway hyperactivity syndromes that are exacerbated by cold (*9*, *10*), further highlighting interest in understanding how these compounds interact with the channel.

TRPM8, like many other TRP subtypes, is a polymodal, nonselective cation channel with substantial permeability to calcium ions ($P_{Ca}^{2+}/P_{Na}^{+} \sim 3$) (*1*). Moreover, cold- or cooling agent–evoked responses show calcium-dependent desensitization (a phenomenon that likely contributes to cold adaptation), and the synthetic "super cooling" agent icilin activates the channel in a calcium-dependent manner (*11*). Indeed, a conserved TRPM channel calcium-binding site has been identified in close proximity to a TRPM8 agonist-binding pocket (*12*–*14*), but whether this site contributes to agonist-evoked desensitization has not been determined.

Recently published TRPM8 structures from the collared flycatcher (cfTRPM8), either ligand-free or in complex with cooling agents and the positive regulator phosphatidylinositol-4,5-bisphosphate (PIP_2), describe the overall architecture of the channel and reveal binding sites for these ligands (*14*, *15*). However, the local resolution of the transmembrane domain in the cryo–electron microscopy (cryo-EM) maps was insufficient for unambiguous and complete model building, and regions corresponding to the selectivity filter and outer pore loop were invisible, limiting our understanding of the molecular mechanisms of channel gating at the selectivity filter or lower gate. To learn how ligand binding and channel gating are coupled, we determined cryo-EM structures of TRPM8 alone or in complex with antagonists or calcium.

Visualizing TRPM8 in distinct conformational states

We found that channels from birds exhibited superior conformational homogeneity compared with other vertebrate species, in agreement with previous studies (*15*). We also found that TRPM8

[1]Department of Physiology, University of California, San Francisco, San Francisco, CA 94143, USA. [2]Department of Biochemistry and Biophysics, University of California, San Francisco, San Francisco, CA 94143, USA. [3]Howard Hughes Medical Institute, University of California, San Francisco, San Francisco, CA 94143, USA.
***Corresponding author. Email: yifan.cheng@ucsf.edu (Y.C.); david.julius@ucsf.edu (D.J.)**

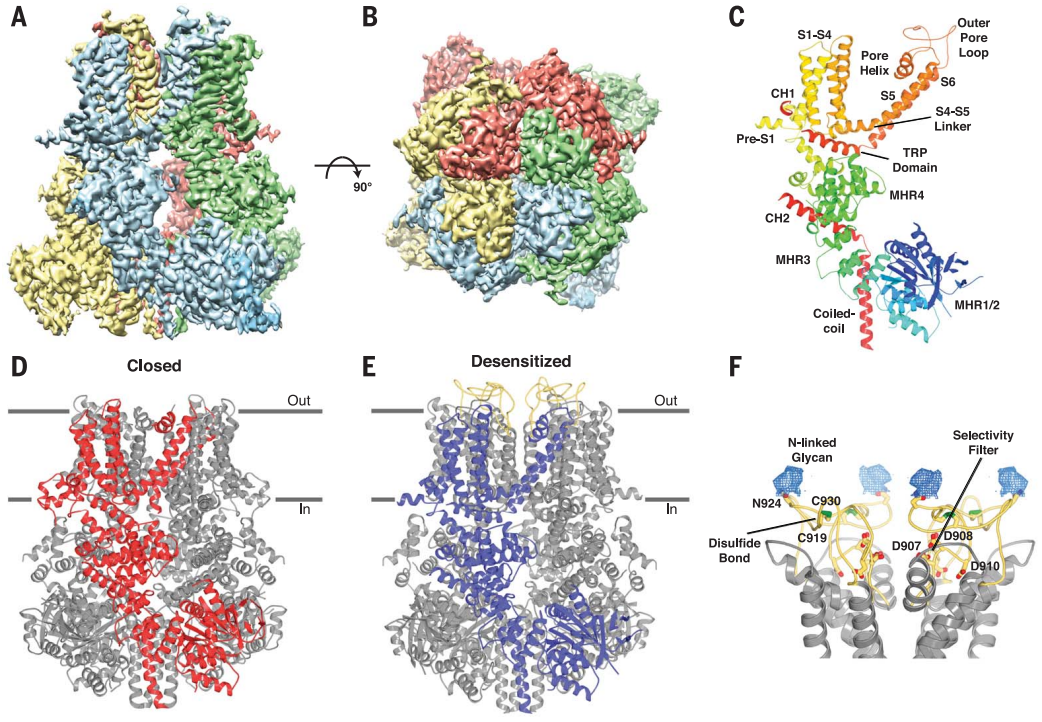

Fig. 1. Structure of TRPM8 in two distinct states. Side view (**A**) and top view (**B**) of the cryo-EM density map of the desensitized state of TRPM8 with subunits differentiated by color. (**C**) Monomer of the desensitized state with secondary structure elements colored blue-to-red from N terminus to C terminus and domains labeled. C-terminal helix 1, CH1; C-terminal helix 2, CH2. (**D**) Ribbon representation of the closed state of TRPM8 (TC-I 2014–bound) with a single subunit colored red. Horizontal lines indicate the approximate boundaries of the cell membrane. (**E**) Ribbon representation of the desensitized state of TRPM8 with a single subunit colored blue. The outer pore loop is colored yellow. (**F**) Close-up view of the outer pore loop. Conserved residues important for selectivity (Asp^{907}, Asp^{908}, and Asp^{910}), disulfide bond formation (Cys^{919} and Cys^{930}), and N-linked glycosylation (Asp^{924}) are drawn as sticks. Nitrogen, blue; oxygen, red; sulfur, green. Density (blue mesh, 4σ contour) for the N-linked glycan is shown. Single-letter abbreviations for the amino acid residues are as follows: A, Ala; C, Cys; D, Asp; E, Glu; F, Phe; G, Gly; H, His; I, Ile; K, Lys; L, Leu; M, Met; N, Asn; P, Pro; Q, Gln; R, Arg; S, Ser; T, Thr; V, Val; W, Trp; and Y, Tyr.

from *Parus major* (great tit; pmTRPM8) produced the highest resolution reconstructions. TRPM8 is remarkably well conserved across vertebrate species, with human and avian orthologs sharing >80 and 85% amino acid sequence identity and similarity, respectively (fig. S1). Recombinant full-length pmTRPM8 protein was purified in detergent supplemented with cholesterol hemisuccinate (CHS) and reconstituted into amphipols. Structures in ligand-free, antagonist-bound (AMTB or TC-I 2014), and calcium-bound states were determined using cryo-EM to average resolutions of 3.6, 3.2, 3.0, and 3.2 Å, respectively (figs. S2 to S9). The cryo-EM density maps are of high quality, allowing for construction of atomic models with good stereochemistry and correlation with the density (Fig. 1, A and B; fig. S10; and table S1).

Overall, our structures conform to the characteristic homotetrameric arrangement described for cfTRPM8 and other TRPM family members, including N-terminal homology regions (MHR1 to MHR4), six transmembrane helices (S1 to S6) arranged in a domain swap architecture, and a C-terminal coiled-coil (Fig. 1 and fig. S11, A to C) (*13*, *15*–*17*). The pore of TRPM8 is formed by S5 and S6, as well as the intervening pore helix and outer pore loop (Fig. 1C). The 44-residue outer pore loop was disordered in the cfTRPM8 structures but is clearly visible in our calcium-bound state (Fig. 1, A to C and E), allowing for the ion conduction pathway to be modeled in its entirety. The pore can be divided into two portions: the negatively charged selectivity filter (fig. S8I) that occupies the outer leaflet of the membrane and the lower gate within the inner

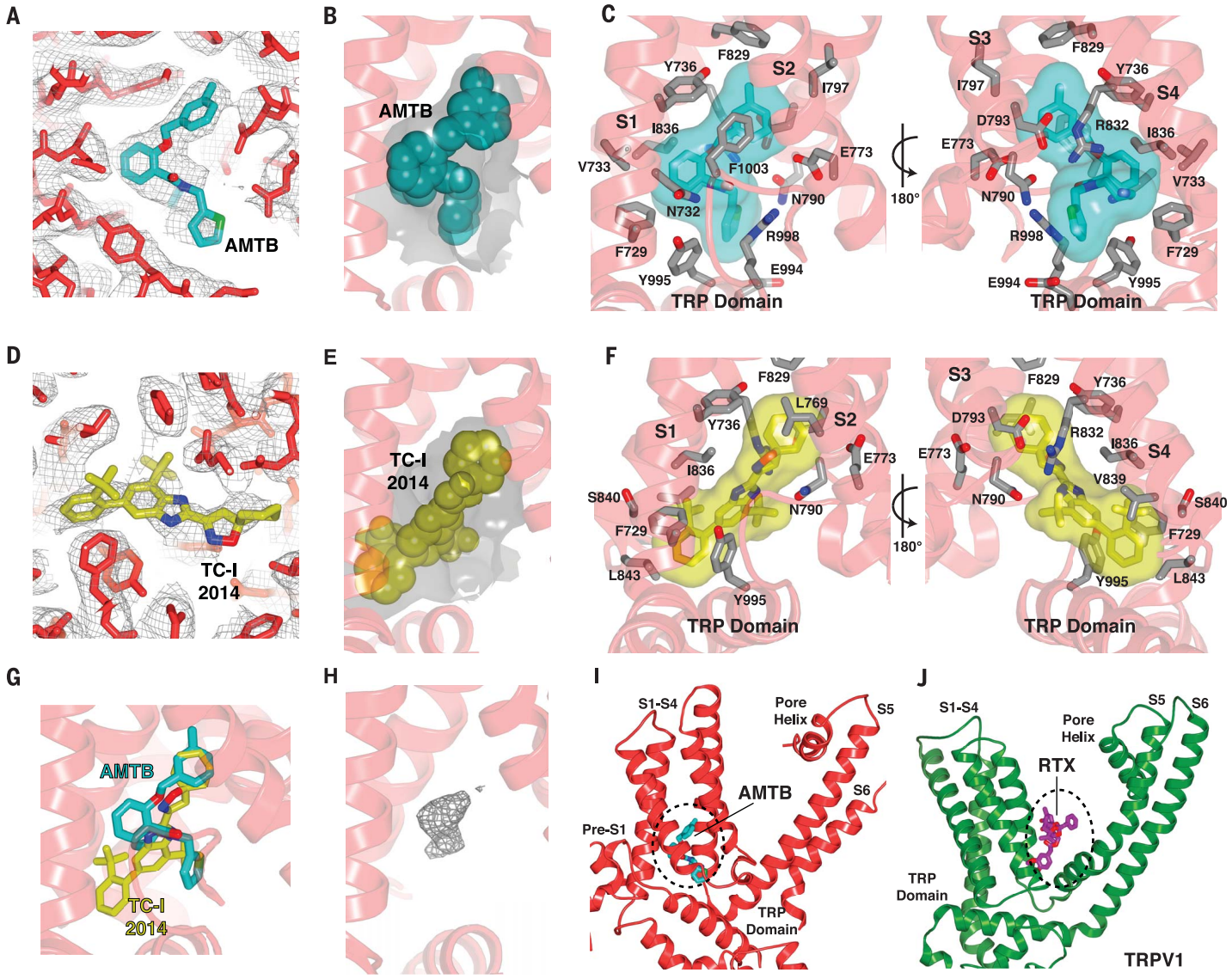

Fig. 2. Binding site for hydrophobic modulators of TRPM8. (**A**) Density within the AMTB-binding site. The map is contoured at 3σ (gray mesh). Stick representation of AMTB-bound TRPM8 with the antagonist AMTB colored teal. (**B**) Gray surface indicates the shape of the binding pocket, as dictated by residues lining the cavity. AMTB is shown as spheres. (**C**) Interactions with AMTB (transparent surface and sticks with teal carbon atoms). Nitrogen, blue; oxygen, red. (**D**) Density within the TC-I 2014–binding site. The map is contoured at 3σ (gray mesh). Stick representation of TC-I 2014–bound TRPM8 with the antagonist TC-I 2014 colored yellow. (**E**) Gray surface indicates the shape of the binding pocket, as dictated by residues lining the cavity. TC-I 2014 is shown as spheres. (**F**) Interactions with TC-I 2014 (transparent surface and sticks with yellow carbon atoms). (**G**) The antagonists AMTB and TC-I 2014 adopt distinct poses in the ligand-binding pocket. (**H**) Unassigned density (gray mesh, 8σ contour) observed in the ligand-binding pocket of ligand-free TRPM8. (**I**) Binding site for hydrophobic modulators in TRPM8. The dashed region demarcates the binding pocket. (**J**) Structure of TRPV1 highlighting the resiniferatoxin (RTX) binding site. The dashed region demarcates the binding site for hydrophobic modulators in TRPV1.

leaflet. The outer pore loop, which is essential for channel functionality, is both disulfide bonded and glycosylated (Fig. 1F) (*18*). Unexpectedly, our structures in distinct conformational states reveal large gating movements, including an unusual formation and dissolution of the S4-S5 linker and a repositioning of the TRP domain. Although we describe the most highly resolved and complete structure obtained for each condition, these likely represent conformational substates sampled by this thermosensitive channel (our final reconstructions are derived from ~3% of particles) (figs. S3, S5, S7, and S9). For example, our dataset obtained in the presence of calcium yielded additional high-resolution structures that indicate heterogeneity within the outer pore loop and the region of calcium binding (S2-S3) (fig. S12).

An adaptable binding pocket for modulators

All known TRPM8 ligands (agonists and antagonists, natural or synthetic) have as their chemical core one or more pentameric or hexameric rings, but they bear a range of substituents (*19*), suggesting that adaptability of the binding pocket is a main determinant of high-affinity binding. To explore this concept further, we determined structures in the presence of two chemically distinct antagonists, AMTB and TC-I 2014 (*20*, *21*) (figs. S4H and S6H), both of which inhibit menthol-evoked responses in oocytes expressing pmTRPM8 (figs. S4I and S6I). The antagonists are nestled in a membrane-embedded cleft formed by the lower half of the S1-S4 domain, near the membrane-cytosol interface, where they are encapsulated in a pocket that is lined by both hydrophobic and charged residues contributed by the S1-S4 helices and the TRP domain (Fig. 2, A to F). Substituents on the rings do not form specific ionic interactions with charged side chains, supporting shape complementarity as the major determinant of ligand recognition (Fig. 2, B, C, E, and F). Furthermore, although both drugs bind within this same pocket, they dock in distinct orientations (Fig. 2G), which is facilitated by complementary rearrangement of

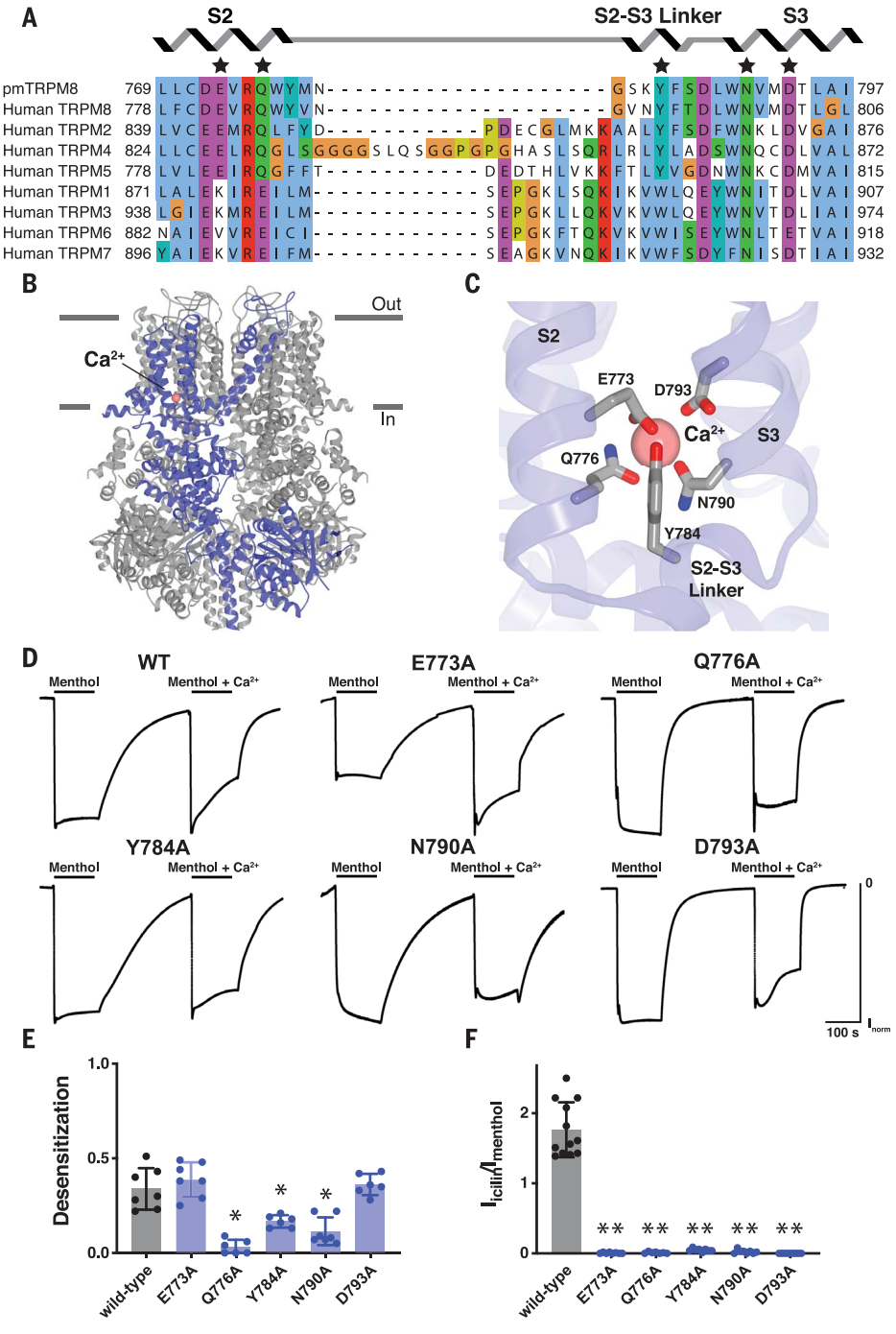

Fig. 3. TRPM8 calcium-binding site.
(**A**) Sequence alignment of the calcium-binding site within the TRPM subfamily. The conserved binding site is shared by TRPM2, TRPM4, TRPM5, and TRPM8. Residues that coordinate the calcium ion are indicated with a star. Alignment was made with ClustalW. (**B**) Ribbon representation of calcium-bound TRPM8 with a single subunit colored blue and the calcium ion colored pink (sphere). Horizontal lines indicate the approximate boundaries of the cell membrane. (**C**) Interactions with calcium (pink sphere). Nitrogen, blue; oxygen, red. (**D** and **E**) Structure-function analysis of the role of the calcium-binding site in TRPM8 desensitization. In oocytes expressing pmTRPM8, application of menthol (100 μM) evoked inward currents for which desensitization was observed in the presence of calcium. However, upon mutating several of the residues important for calcium coordination, TRPM8 desensitization was reduced. The A796G mutation was introduced to all constructs to sensitize avian TRPM8 to the agonist icilin. Voltage was held at −60 mV. Desensitization is reported as $I_{final}/I_{initial}$ (maximum currents ranged from 0.5 to 4 mA) for the application of menthol in the presence of calcium. Data represent n = 6 or 7 oocytes. Asterisk indicates $P < 0.01$ comparing wild type and each mutant construct with unpaired two-tailed Student's t-tests. Representative traces are shown in (D). (**F**) Structure-function analysis of the role of the calcium-binding site in coagonism with icilin. In oocytes expressing pmTRPM8, application of menthol (100 μM) or icilin (10 μM), in the presence of calcium, evoked inward currents. However, upon mutating residues proposed to be important for calcium coordination, there was no longer a response to icilin. The A796G mutation was introduced to all constructs to sensitize avian TRPM8 to the agonist icilin. Voltage was held at −60 mV. Data represent n = 7 to 12 oocytes. Two asterisks indicate $P < 1 \times 10^{-8}$ comparing wild type and each mutant construct with unpaired two-tailed Student's t-tests.

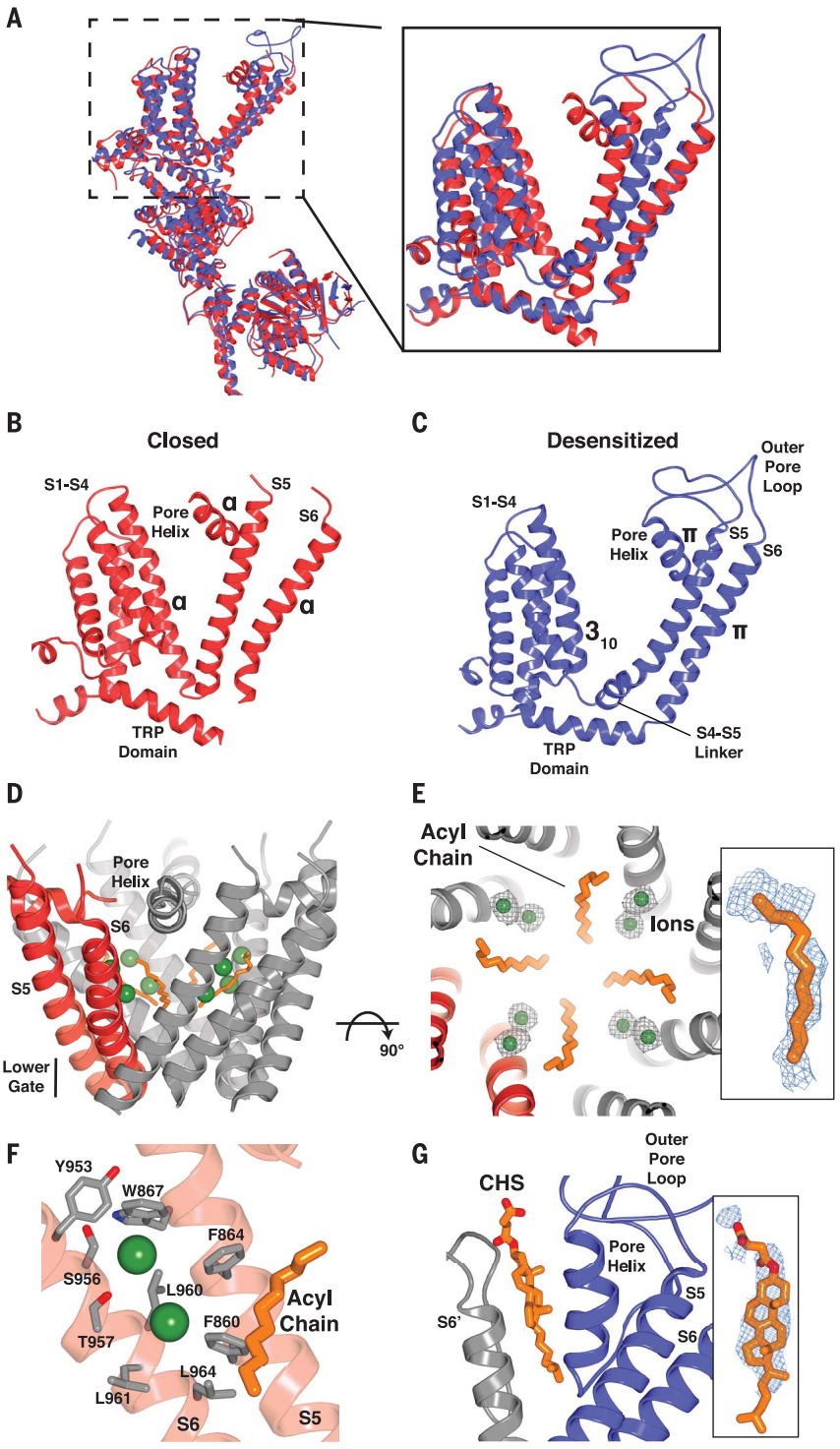

Fig. 4. Conformational changes associated with ligand binding to a shared pocket. (**A**) Superimposition of the closed (TC-I 2014–bound; red) and desensitized (blue) TRPM8 structures. (**B** and **C**) Structural changes associated with TRPM8 channel gating. Transition from the closed (B) to desensitized (C) state is accompanied by formation of a S4-S5 linker, a local α-to-π-helical transition in S6, and rearrangement of the TRP domain, which alter the lower gate. (**D**) In the closed state, an ordered acyl chain (orange) is present along the ion permeation pathway, thereby increasing the hydrophobicity of the pore. Green spheres indicate ions observed in the vicinity of the acyl chains. (**E**) Close-up view, orthogonal to (D) with ion densities (gray mesh; 3σ contour). Inset shows density for acyl chain (blue mesh, 3σ contour). (**F**) Cation binding sites (green spheres) are in close proximity to negatively charged residues contributed by S6. Nitrogen, blue; oxygen, red. (**G**) In the desensitized state, a stabilizing lipid packs between the pore helix and S6 of the neighboring subunit (modeled as CHS). Inset shows lipid density (blue mesh, 4σ contour).

the side chains that define cavity shape. This ligand-binding pocket also accommodates agonists (although their precise binding orientations were not ascertained) (*14*) (fig. S13, A and B). The overall structure of TRPM8 remains unaltered in ligand-free or antagonist-bound maps, suggesting that these chemically distinct inhibitors mediate their effects by binding to this promiscuous pocket and locking the channel in its ligand-free configuration.

In the absence of an exogenous ligand, we observed a discrete density in the ligand-binding pocket (Fig. 2H). Although we cannot identify the molecule corresponding to this density, its presence suggests that ligands do not bind to an empty cavity but rather displace an endogenous molecule. This observation may have potential physiologic significance and is important to bear in mind when assigning density in this location to an exogenous ligand. Furthermore, this finding is reminiscent of the vanilloid-binding pocket in TRPV1, which is occupied by a phosphatidylinositol lipid in its apo state (*22*, *23*). This similarity notwithstanding, the location of the TRPM8 ligand-binding pocket is distinct from that described for other TRP channels. For example, vanilloid ligands bind to TRPV1 in an elbow between the S1-S4 and S5-S6 domains and above the S4-S5 linker (Fig. 2, I and J) (*22*, *23*), and nucleotide ligands bind within cytoplasmic regions of TRPM2 and TRPM4 (fig. S11, A and B) (*13*, *16*).

Structural mechanism of calcium-dependent modulation

TRPM8 currents show pronounced calcium-dependent desensitization during continuous agonist application (*11*). We therefore determined the structure of TRPM8 in the presence of calcium to identify the major site(s) of interaction and ascertain whether divalent cation binding is associated with specific conformations, particularly a desensitized state. We found that calcium is bound in a manner analogous to that previously described for a subset of TRPM channels (fig. S11, A and B) (*12*–*14*), whereby the ion is coordinated by four negatively charged residues (Glu^{773}, Gln^{776}, Asn^{790}, and Asp^{793}) from the S2 and S3 transmembrane helices (Fig. 3, A to C), adjacent to the ligand-binding pocket described above. We also observed involvement of a fifth side chain belonging to Tyr^{784} within the S2-S3 linker (Fig. 3, A and C).

To determine whether this calcium-binding site is responsible for calcium-dependent desensitization, we analyzed menthol-evoked responses for TRPM8 channels bearing alanine substitutions at the identified calcium-binding residues (Fig. 3, D and E). Several of these mutations diminished desensitization, with the most pronounced effects associated with Gln^{776} and Asn^{790}, the acidic residues that form the base of the binding site. By introducing a Ala^{796}→Gly (A796G) mutation into pmTRPM8 (a modification that renders avian TRPM8 icilin-sensitive) (*11*), we could also show that all five calcium-binding residues are required for icilin sensitivity (Fig. 3F). Mutation of Glu^{773} and Asp^{793}

abrogated icilin-evoked responses without impairing desensitization, suggesting that these actions require high and low calcium-binding affinities, respectively.

Conformational states associated with ligand and lipid binding

Our high-quality maps (~2.5 to 3 Å in the transmembrane domain) are sufficient to allow for unambiguous placement of all residues in S1-S6, enabling us to define two distinct conformational states of TRPM8: a closed state in the presence of an antagonist and a desensitized state in the presence of an agonist (cold) and calcium (Fig. 4). With the improved map quality, we can correct previous assignment of the lower gate in the closed state from Leu^{973} (Leu^{964} in pmTRPM8) (*14*, *15*) to an extended restriction comprising two hydrophobic residues, Met^{968} and Phe^{969} (Fig. 5, A to C and E). In the presence of antagonists, we also observed a lipid tail protruding into the ion conduction pathway, where it forms a hydrophobic barrier that narrows the ion permeation path to ~3 Å in diameter (Figs. 4, D to F, and 5, B, C, and E). Indeed, we see ions collecting at this constriction (Fig. 4, D and E), which is consistent with the idea that lipids create a vestibule below the selectivity filter, where ions accumulate along a negatively charged face of S6 when the channel is closed (Fig. 4F). This is reminiscent of two-pore domain potassium channels, some voltage-dependent sodium channels, and mitochondrial calcium uniporters, where lipids similarly form a hydrophobic barrier along the ion conduction pathway (*24*–*26*). Another unusual feature of the closed state is lack of a canonical S4-S5 linker (Fig. 4B), which plays a critical role in activation of voltage-gated channels (*27*) but is relatively static in TRP channel structures reported to date (*28*).

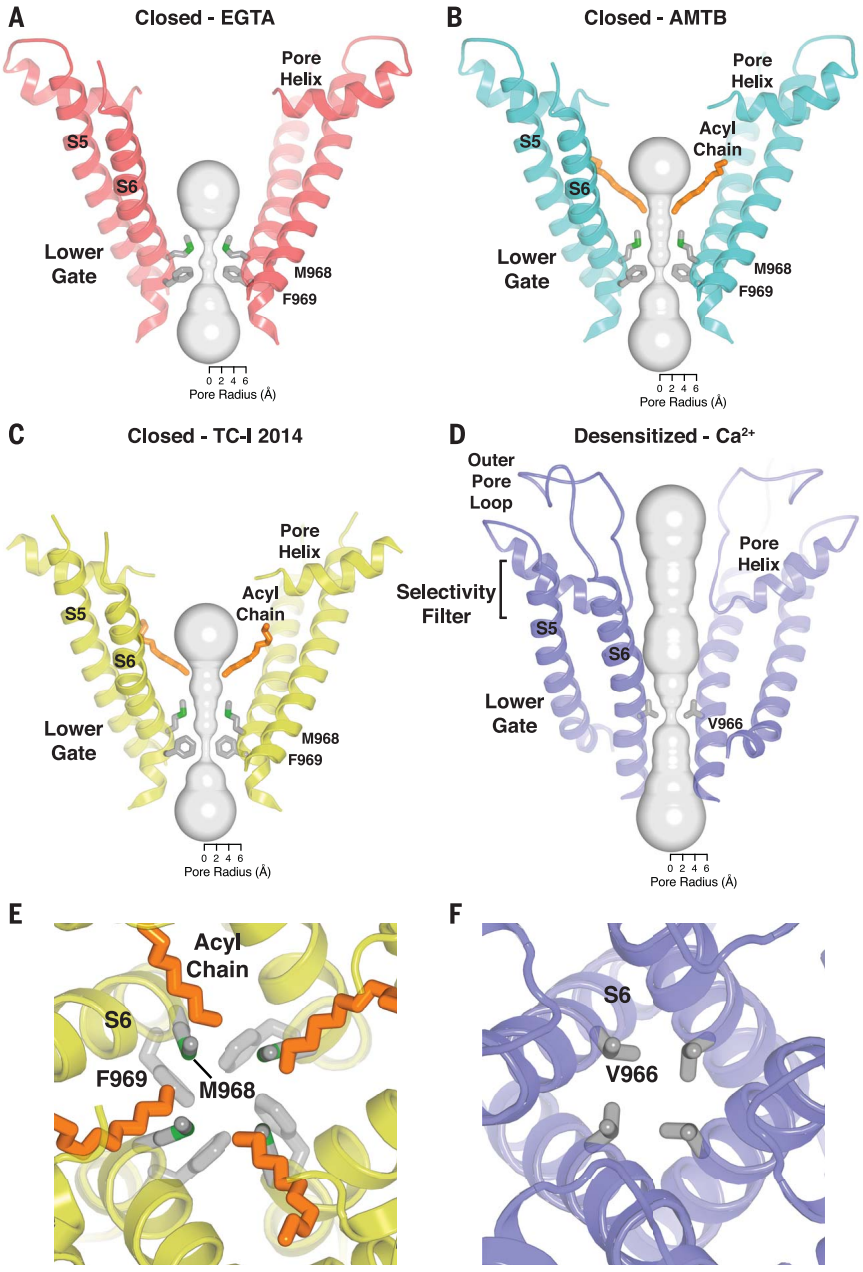

Fig. 5. Ion pore. (**A** to **D**) Ion conduction pathway with front and rear subunits removed for clarity and a representation (gray surface) of the minimal radial distance from the center of the pore to the nearest van der Waals protein or lipid contact. Residues lining the selectivity filter and lower gate are shown as sticks for the EGTA-bound (A), AMTB-bound (B), TC-I 2014–bound (C), and calcium-bound (D) states. (**E** and **F**) Close-up view of the lower gate of closed (TC-I 2014–bound) (E) and desensitized (F) TRPM8. The residues and acyl chain (closed conformation only) that form the hydrophobic seal are shown as sticks.

In contrast to the closed TRPM8 structure, our desensitized structure shows the typical S4-S5 linker architecture seen in other TRP channels (Fig. 4C). In this desensitized state, we see that the side chain from a single hydrophobic residue (Val^{966}) reduces the radius of the lower gate to <1 Å (Fig. 5, D and F). In other TRPM channel conformations with similar overall architecture (fig. S11, A to C), the lower gate is formed by two residues, producing a more extended restriction, which is consistent with these structures representing the closed state (fig. S11, D to F) (*16*, *17*, *29*). Introduction of a positively charged residue at this position in TRPM2 (I1045K) or TRPM8 (V966K) is reported to alter ion selectivity, as would be expected if this residue plays a critical role in controlling ion permeation (*30*). We posit that this minimal, efficient constriction in the presence of calcium defines the desensitized state of TRPM8. We also found that the outer pore loop is structurally resolved in this state, where the presence of calcium induces a large rearrangement leading to the formation of an exposed crevice between the pore helix and S6 of an adjacent subunit. This crevice is occupied by a lipid, modeled as CHS on the basis of the characteristic shape of its density (Fig. 4G), which presumably stabilizes the outer pore domain in this functional state.

Another notable feature (of both states) pertains to the packing of lipids at subunit interfaces, where they are cradled by the pre-S1 elbow and S1 helix of one subunit and the S5 helix of its neighbor (fig. S14). In this pocket, we observed a mixture of lipids, including some that can be modeled as CHS. PIP_2, a modulator of TRPM8 function (*31*, *32*), has recently been speculated (*33*) and shown (*14*) to bind in this pocket. Whereas a single lipid molecule has been observed in this location for other TRP channels containing a similar pre-S1 elbow (*12*, *34*, *35*), here we see clusters of lipids occupying the entire region. In the closed conformation in which the cavity is larger, more lipid molecules were observed (fig. S14). Cryo-EM image processing suggests that the transmembrane domain of

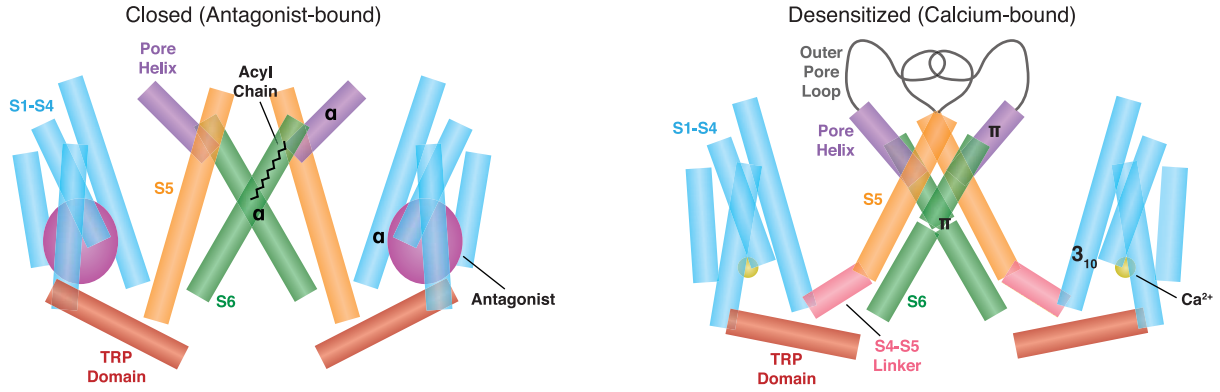

Fig. 6. Gating movements in TRPM8. In the presence of antagonists (left panel), TRPM8 is closed and density corresponding to an acyl chain is present within the ion conduction pathway. In the presence of calcium (right panel), the channel is desensitized. Structural rearrangements associated with transitioning from closed to desensitized states include a rigid-body tilt of the S1-S4 domain; formation of a canonical S4-S5 linker; shifts of S5, the pore helix, and S6; stabilization of the outer pore loop; and tilting of the TRP domain, such that it is parallel to the membrane bilayer. This transition is accompanied by introduction of a 3_{10} helix in S4 and a π helix in both the pore helix and S6.

TRPM8 is very conformationally dynamic (figs. S3, S5, S7, and S9), and this tight packing of well-ordered lipids may have enhanced channel stability for structure determination.

Ligand-induced TRPM8 gating movements

By modeling the transition from the closed to desensitized state, we observed a constellation of conformational changes that provide insight into TRPM8 gating mechanisms (Figs. 4, A to C, and 6). First, as previously observed upon binding of icilin (*14*), the S1-S4 domain undergoes a rigid-body tilt away from the central axis that is accompanied by transition of an α-helical turn in S4 (Thr^{830} to Arg^{832}) to a 3_{10} helix (Figs. 4, A to C, and 6). We now show that this transition is stabilized by several interactions (Arg^{832} forms ionic bonds with Tyr^{736} and Asp^{793}; His^{835} stacks with Trp^{789}) and leads to formation of a canonical S4-S5 linker (Figs. 4, A to C, and 6). This is accompanied by large shifts of S5, the pore helix (including introduction of a π helix), and S6, pivoting these regions into the central pathway (Figs. 4, A to C, and 6) and adopting an overall conformation distinct from the icilin-PIP_2-calcium–bound structure (fig. S13C) (*14*), but resembling that observed for other TRP channels. Furthermore, the previously disordered and invisible outer pore loop (*14*, *15*) is now stabilized and well resolved (Figs. 4, A to C, and 6), perhaps reflecting its conformationally dynamic nature, reminiscent of TRPV1, another temperature-sensitive channel (*22*). This is consistent with the fact that the loop is not seen in all subclasses of the desensitized state (fig. S12).

In comparing our two states, we also see interesting rearrangements near the lower gate (Figs. 4, A to C, and 6). For example, the section spanning residues Ser^{956} to Leu^{961} in S6 undergoes a transition from an α helix to π helix, shifting the register of the lower gate and reducing the constriction at the hydrophobic seal—a structural mechanism underlying channel opening in some TRPV channels (*36*, *37*). Finally, a large tilting movement (~25°) is seen in the conserved and functionally essential TRP domain, rendering it parallel to the membrane bilayer (Figs. 4, A to C, and 6). The TRP domain is known to play an important role in the allosteric modulation of many TRP channel family members (*28*). Furthermore, the TRP domain is stacked between the overlying S4-S5 linker and the underlying MHR4 domain within the cytoplasmic N terminus, resembling the highly integrated allosteric nexus observed in the TRPA1 channel (*38*). Whether this arrangement reflects a mechanism by which TRPM8 detects and/or integrates cytoplasmic signals remains to be determined.

Close inspection of the S1-S4 ligand-binding pocket provides mechanistic insight into how the binding of modulators promotes key conformational transitions, including movements of the TRP domain and the S4-S5 linker, which control the lower gate. For example, the antagonist TC-I 2014 nestles deep within a pocket present only in the closed state that is formed in part by residues of S4 and the TRP domain (fig. S15A). Features of the closed state (i.e., absence of the S4-S5 linker and relative position of the TRP domain) allow antagonists to lock the channel in this closed conformation. In the desensitized state, the pocket, as defined by these interactions, dissolves and cannot accommodate antagonist molecules (fig. S15A), but it can be fit by icilin (*14*). Thus, we conclude that the ligand-binding pocket associated with closed or open states primarily reflects the position of the TRP helix relative to S1-S4 rather than intrinsic rearrangements to the S1-S4 domain. This is reminiscent of gating movements recently described for TRPM2, where TRP helix movement is also observed but initiated from below by binding of an activator to the soluble domain (*13*). Furthermore, comparison of our structures in EGTA- and calcium-bound states shows why calcium stabilizes the desensitized state: its binding disrupts an important ionic interaction between Arg^{998} (TRP domain) and Gln^{776} (S2 helix), enabling the TRP domain to assume the location described above for the desensitized state (fig. S15B).

Discussion

Calcium plays a multifaceted role in TRP channel physiology, serving as a cofactor for stimulus-evoked gating and/or desensitization (*39*). In regard to the latter, it remains unknown for many TRP subtypes whether desensitization is mediated through direct interaction of calcium with the channel, by auxiliary proteins such as calmodulin, or via calcium-sensitive pathways such as phospholipase C–mediated depletion of PIP_2 (*32*, *40*). Our results demonstrate that desensitization of TRPM8 occurs through direct calcium binding at a site that is conserved among a subset of TRPM channels. Calcium binding to this same site is also required for activation by icilin, consistent with the fact that icilin-evoked responses always desensitize. This stands in contrast to some TRPV channel subtypes, where calmodulin is the effector for calcium-mediated desensitization (*41*). We have shown that closed and desensitized states define distinct conformational rearrangements. Although structures corresponding to open states have been difficult to visualize for TRP channels, we propose that the calcium-bound, nonconducting desensitized structure described here closely resembles the TRPM8 open state, except for closure of the gate by a single hydrophobic residue (Val^{966}) as a minimal energetic step defining this transition. However, it is also possible that the open state is unrelated, but sufficiently unstable for structural characterization, perhaps explaining why the closed state is observed even in the presence of cold or cooling compounds (*14*). Ultimately, visualization of all major functional states will be required to unequivocally assign specific structures to precise physiological states.

Our results support an emerging concept in which TRP channels fall nominally into two main classes, one exemplified by TRPV and TRPML subtypes that show relatively modest conformational changes associated with distinct functional states (*22*, *36*, *37*, *41*–*44*), and another represented by TRPM subtypes, in which much larger conformational changes are observed

throughout the protein (*13*, *22*). Studies of TRPV and TRPML channels show that the S1-S4 domain remains stationary during channel opening, and ligands bind between this domain and the pore region (S5-S6) to affect gating (*22*, *36*, *37*, *41*–*44*). This stands in contrast to voltage-gated channels, where channel opening is promoted by conformational rearrangements within the S1-S4 domain (*45*). Our results show that TRPM8 channels exhibit an intermediate behavior in which ligands (agonists, antagonists, and calcium) bind within the S1-S4 domain to alter its position relative to the TRP helix without changing its overall structure. At the same time, thermosensitive TRPM8 and TRPV1 channels show dynamic conformational changes within the outer pore region, which has been implicated in sensing chemical and thermal stimuli (*46*–*48*).

Both agonists and antagonists of TRPM8 have sensorial and therapeutic applications (*49*), with antagonists being explored for management of cold hypersensitivity associated with neuropathic pain (*50*). Our structures suggest that the ligand-binding pocket is malleable and can adopt different contours through subtle side-chain movements to accommodate a range of small molecule structures and orientations. This local flexibility might be exploited to introduce moieties that enhance drug stability, solubility, or availability. It is also intriguing to see a density in the ligand-binding pocket in the absence of an exogenous ligand, and it will be interesting to determine the identity of this agent and whether it behaves as a stabilizing cofactor, a natural antagonist, or an inverse agonist. In any case, our findings provide a mechanistic rationale for understanding how ligands affect channel gating, which may facilitate the design of drugs that selectively modulate aberrant channel activity under pathophysiological conditions.

REFERENCES AND NOTES

1. D. D. McKemy, W. M. Neuhausser, D. Julius, *Nature* **416**, 52–58 (2002).
2. A. M. Peier *et al*., *Cell* **108**, 705–715 (2002).
3. D. M. Bautista *et al*., *Nature* **448**, 204–208 (2007).
4. A. Dhaka *et al*., *Neuron* **54**, 371–378 (2007).
5. R. W. Colburn *et al*., *Neuron* **54**, 379–386 (2007).
6. S. S. Bharate, S. B. Bharate, *ACS Chem. Neurosci.* **3**, 248–267 (2012).
7. H. Xing, M. Chen, J. Ling, W. Tan, J. G. Gu, *J. Neurosci.* **27**, 13680–13690 (2007).
8. J. Descoeur *et al*., *EMBO Mol. Med.* **3**, 266–278 (2011).
9. S. J. Bonvini, M. G. Belvisi, *Pulm. Pharmacol. Ther.* **47**, 21–28 (2017).
10. H. Liu, Q. Liu, L. Hua, J. Pan, *Acta Biochim. Biophys. Sin. (Shanghai)* **50**, 499–506 (2018).
11. H.-H. Chuang, W. M. Neuhausser, D. Julius, *Neuron* **43**, 859–869 (2004).
12. H. E. Autzen *et al*., *Science* **359**, 228–232 (2018).
13. Y. Huang, P. A. Winkler, W. Sun, W. Lü, J. Du, *Nature* **562**, 145–149 (2018).
14. Y. Yin *et al*., *Science* **363**, eaav9334 (2019).
15. Y. Yin *et al*., *Science* **359**, 237–241 (2018).
16. J. Guo *et al*., *Nature* **552**, 205–209 (2017).
17. J. Duan *et al*., *Proc. Natl. Acad. Sci. U.S.A.* **115**, E8201–E8210 (2018).
18. M. Pertusa, R. Madrid, C. Morenilla-Palao, C. Belmonte, F. Viana, *J. Biol. Chem.* **287**, 18218–18229 (2012).
19. V. B. Journigan, N. T. Zaveri, *Life Sci.* **92**, 425–437 (2013).
20. E. S. R. Lashinger *et al*., *Am. J. Physiol. Renal Physiol.* **295**, F803–F810 (2008).
21. D. J. Parks *et al*., *J. Med. Chem.* **54**, 233–247 (2011).
22. E. Cao, M. Liao, Y. Cheng, D. Julius, *Nature* **504**, 113–118 (2013).
23. Y. Gao, E. Cao, D. Julius, Y. Cheng, *Nature* **534**, 347–351 (2016).
24. A. N. Miller, S. B. Long, *Science* **335**, 432–436 (2012).
25. J. Payandeh, T. Scheuer, N. Zheng, W. A. Catterall, *Nature* **475**, 353–358 (2011).
26. R. Baradaran, C. Wang, A. F. Siliciano, S. B. Long, *Nature* **559**, 580–584 (2018).
27. S. B. Long, E. B. Campbell, R. Mackinnon, *Science* **309**, 897–903 (2005).
28. M. G. Madej, C. M. Ziegler, *Pflugers Arch.* **470**, 213–225 (2018).
29. Z. Zhang, B. Tóth, A. Szollosi, J. Chen, L. Csanády, *eLife* **7**, e36409 (2018).
30. F. J. P. Kühn, G. Knop, A. Lückhoff, *J. Biol. Chem.* **282**, 27598–27609 (2007).
31. B. Liu, F. Qin, *J. Neurosci.* **25**, 1674–1681 (2005).
32. T. Rohács, C. M. B. Lopes, I. Michailidis, D. E. Logothetis, *Nat. Neurosci.* **8**, 626–634 (2005).
33. W. Zheng *et al*., *Cell Rep.* **22**, 1560–1573 (2018).
34. P. Jin *et al*., *Nature* **547**, 118–122 (2017).
35. C. Fan, W. Choi, W. Sun, J. Du, W. Lü, *eLife* **7**, e36852 (2018).
36. L. L. McGoldrick *et al*., *Nature* **553**, 233–237 (2018).
37. A. K. Singh, L. L. McGoldrick, A. I. Sobolevsky, *Nat. Struct. Mol. Biol.* **25**, 805–813 (2018).
38. C. E. Paulsen, J.-P. Armache, Y. Gao, Y. Cheng, D. Julius, *Nature* **520**, 511–517 (2015).
39. R. Hasan, X. Zhang, *Int. J. Mol. Sci.* **19**, 1256 (2018).
40. I. Sarria, J. Ling, M. X. Zhu, J. G. Gu, *J. Neurophysiol.* **106**, 3056–3066 (2011).
41. T. E. T. Hughes *et al*., *Nat. Commun.* **9**, 4198 (2018).
42. T. L. Dosey *et al*., *Nat. Struct. Mol. Biol.* **26**, 40–49 (2019).
43. P. Schmiege, M. Fine, G. Blobel, X. Li, *Nature* **550**, 366–370 (2017).
44. X. Zhou *et al*., *Nat. Struct. Mol. Biol.* **24**, 1146–1154 (2017).
45. K. J. Swartz, *Nature* **456**, 891–897 (2008).
46. V. Matos-Cruz *et al*., *Cell Rep.* **21**, 3329–3337 (2017).
47. J. Grandl *et al*., *Nat. Neurosci.* **13**, 708–714 (2010).
48. M. Pertusa, B. Rivera, A. González, G. Ugarte, R. Madrid, *J. Biol. Chem.* **293**, 12454–12471 (2018).
49. W. M. Knowlton, D. D. McKemy, *Curr. Pharm. Biotechnol.* **12**, 68–77 (2011).
50. A. D. Weyer, S. G. Lehto, *Pharmaceuticals* **10**, 37–39 (2017).

ACKNOWLEDGMENTS

We thank Y. Guo and J. Osteen for their contributions to initial stages of this project; members of the Cheng and Julius laboratories for discussions; and the staff of the Keck Advanced Microscopy Laboratory of the University of California, San Francisco, D. Bulkley and A. Myasnikov, for help with data collection. **Funding:** This work was supported, in part, by an A.P. Giannini Foundation Postdoctoral Fellowship (M.M.D.) and by grants from the National Institutes of Health (R35NS105038 to D.J. and R01GM098672, S10OD020054, and S10OD021741 to Y.C.). Y.C. is an investigator of the Howard Hughes Medical Institute. **Author contributions:** M.M.D. designed and executed experiments, including protein expression and purification, cryo-EM data acquisition and image processing, atomic model building and refinement of TRPM8 structures, as well as oocyte electrophysiology. Y.C. and D.J. provided advice and guidance throughout. All authors contributed to preparation of the manuscript. **Competing interests:** The authors declare no competing interests. **Data and materials availability:** Cryo-EM density maps have been deposited to the Electron Microscopy Data Bank (EMDB) under the accession numbers EMD-0631 (ligand-free TRPM8), EMD-0636 (AMTB-bound TRPM8), EMD-0638 (TC-I 2014–bound TRPM8), and EMD-0639 (calcium-bound TRPM8). Atomic coordinates have been deposited in the Protein Data Bank under IDs 6O6A (ligand-free TRPM8), 6O6R (AMTB-bound TRPM8), 6O72 (TC-I 2014–bound TRPM8), and 6O77 (calcium-bound TRPM8). All DNA constructs described in this study are available upon request.

SUPPLEMENTARY MATERIALS

science.sciencemag.org/content/365/6460/1434/suppl/DC1
Materials and Methods
Figs. S1 to S15
Table S1
References (*51*–*66*)

11 April 2019; accepted 26 August 2019
Published online 5 September 2019
10.1126/science.aax6672